International Journal of
Plasma Environmental Science and Technology

Regular Paper DOI: 10.34343/ijpest.2026.20.e01004

Simulation of VOC decomposition using direct and indirect nonthermal plasma

Masaaki Okubo[1,*], Tomoyuki Kuroki[1], Haruhiko Yamasaki[1], Koji Ozawa[2], Kazuhiko Kamiya[2]

[1] Department of Mechanical Engineering, Osaka Metropolitan University, Japan
[2] Overseas Market Development Department, Karumoa Co., Ltd., Japan

* Corresponding author: mokubo@mokubo.com (Masaaki Okubo)

Received: 28 October 2025
Revised: 22 December 2025
Accepted: 8 February 2026
Published online: 17 February 2026

Abstract

To provide design guidance for volatile organic compound (VOC) abatement devices, we numerically simulate VOC decomposition in atmospheric-pressure air using direct (in-reactor) and indirect (plasma-injection) nonthermal plasma methods via Microsoft Excel Visual Basic for Applications, and compare predictions with experimental results. Sixteen chemical species, including electrons, are considered for the air plasma with diluted VOC, integrated with a 33-reaction kinetic mechanism to simulate transient species evolutions. The direct-plasma model was calibrated to published toluene ($C_6H_5CH_3$) decomposition data from a coaxial dielectric-barrier-discharge reactor and then transferred, without further tuning, to predict the performance of the indirect plasma-injection configuration for VOC of allyl disulfide ($C_6H_{10}S_2$). Across four tubular-channel regions, simulations capture ozone formation and VOC decomposition trends, yielding predicted outlet concentrations as well as other radical components. The experimental VOC removal efficiency (77.5%–83.7%) agrees qualitatively with the calculated data (83.7%–99.9%).

Keywords: Volatile organic compound, nonthermal plasma, ozone, hydroxyl radical, indirect plasma.

1. Introduction

Volatile organic compounds (VOCs) and fine particulate matter ($PM_{2.5}$) are carcinogenic, leading to the well-known sick building syndrome. In environments where these substances are common, such as the painting and printing industries, and where they are also emitted from ships [1], stringent environmental regulations have been imposed. Conventional VOC removal methods, such as photocatalysis, thermal catalysis [2–4], adsorption [5], and biofiltration [6], are limited by their reliance on precious metals, high operating costs, significant energy consumption, and poor adaptability to flow rate fluctuations. By contrast, nonthermal plasma (NTP) methods [7–13] can remove a wide range of pollutants at room temperature and pressure with little to no maintenance or operating costs. The most common NTP methods (i.e., electric air cleaners and VOCs) have been studied quite extensively [14–36]. However, numerical prediction models remain scarce. To fill this gap, this study simulates VOC decomposition via direct and indirect plasma injection methods using air plasma at atmospheric pressure. We compare experimental and predicted results for ozone production and capture a variety of VOC decomposition efficiency values. The simulation incorporates relevant chemical reactions and rate coefficients for the decomposition of allyl disulfide ($C_6H_{10}S_2$), a key food-odor components responsible for the characteristic garlic smell. The numerical analysis reproduces the conditions of allyl disulfide decomposition experiments.

2. Chemical reactions and calculation method

2.1 Chemical species and chemical reactions with rate coefficients

The following 14 chemical species are considered, including the VOC decomposed products and byproducts: O_3, N_2, H_2O, $N_2(A^3\Sigma_u^+) = N_2(A)$, $N_2(a^1\Sigma_u^-) = N_2(a)$, $N_2(B^3\Pi_g) = N_2(B)$, $N_2(C^3\Pi_u) = N_2(C)$, H_2O, H, OH, NO, N, VOC (C_7H_8 or $C_6H_{10}S_2$), products. The concentrations of these species are expressed with y_1–y_{14}. The chemical reactions of air plasma, which have been considered, are shown in Table 1, referring to National Institute of Standards and Technology (NIST) database [37] and literature [38–56]. The Arrhenius-type reaction rate coefficient is determined in the table. We calculate the collision cross-sections referring to the literature. The collision cross sections mean the electron–molecule collision cross sections $\sigma(E)$ as a function of energy E for reactions R1, R4, R6, R7, and R21. They are used to calculate the corresponding electron-impact rate coefficients k_1, k_4, k_6, k_7, and k_{21} in the kinetic model. Each k_i (i = 1, 4, 6, 7, and 21) is obtained by numerically integrating the product $\sigma_i(E)v(E)f(E)$ over electron energy using tabulated $\sigma(E)$ data, assuming a Gaussian-type electron energy distribution function with an assumed constant electron temperature of T_e = 1.5 eV. In this study, the following reaction rate equation is used as a first-order reaction. Diffusion coefficients are not considered because they are unknown.

2.2 Reaction rate equations

The time evolution of reactions listed in Table 1 is governed by Eqs. (1)–(77), below. For these reactions, concentrations of oxygen ($O_2 = y_1$), electrons ($e = y_2$), nitrogen ($N_2 = y_5$), and water vapor ($H_2O = y_{10}$) are assumed constant.

Oxygen:

$$R_1: \quad \frac{dy_3}{dt} = 2k_1 y_2 y_1 \tag{1}$$

$$R_2: \quad \frac{dy_4}{dt} = k_2 y_3 y_1^2, \quad \frac{dy_3}{dt} = -k_2 y_3 y_1^2 \tag{2}$$

$$R_3: \quad \frac{dy_4}{dt} = -k_3 y_3 y_4 = \frac{dy_3}{dt} \tag{3}$$

$$R_4: \quad \frac{dy_3}{dt} = k_4 y_4 y_2, \quad \frac{dy_4}{dt} = -k_4 y_4 y_2 \tag{4), (5}$$

$$R_5: \quad \frac{dy_4}{dt} = k_5 y_3 y_1 y_5, \quad \frac{dy_3}{dt} = -k_5 y_3 y_1 y_5, \quad \frac{dy_5}{dt} = k_5 y_3 y_1 y_5 - k_5 y_3 y_1 y_5 = 0 \tag{6), (7), (8}$$

Electron:

$$R_6: \quad \frac{dy_6}{dt} = k_6 y_2 y_5, \quad \frac{dy_5}{dt} = -k_6 y_2 y_5 \tag{9), (10}$$

$$R_7: \quad \frac{dy_7}{dt} = k_7 y_2 y_5, \quad \frac{dy_5}{dt} = -k_7 y_2 y_5 \tag{11), (12}$$

N_2*:

$$R_8: \quad \frac{dy_5}{dt} = k_8 y_6 y_5, \quad \frac{dy_6}{dt} = -k_8 y_6 y_5 \tag{13), (14}$$

Table 1. Chemical reactions considered.

	Reactions			Rate coefficient		Refs.
O_2	$e + O_2$	→	$O + O + e$	$k_1 = 1.950 \times 10^{-15}$ m^3 molecules^{-1} s^{-1}	R1	[38]
	$O + O_2 + O_2$	→	$O_3 + O_2$	$k_2 = 6.032 \times 10^{-46}$ m^6 molecules^{-2} s^{-1}	R2	[37]
	$O + O_3$	→	$O_2 + O_2$	$k_3 = 8.673 \times 10^{-21}$ m^3 molecules^{-1} s^{-1}	R3	[37]
	$e + O_3$	→	$O + O_2 + e$	$k_4 = 3.900\times 10^{-14}$ m^3 molecules^{-1} s^{-1}	R4	[38]
	$O + O_2 + N_2$	→	$O_3 + N_2$	$k_5 = 6.032 \times 10^{-46}$ m^6 molecules^{-2} s^{-1}	R5	[37]
e	$e + N_2$	→	$N_2(A) + e$	$k_6 = 2.070 \times 10^{-18}$ m^3 molecules^{-1} s^{-1}	R6	[40, 41]
	$e + N_2$	→	$N_2(a) + e$	$k_7 = 7.200 \times 10^{-18}$ m^3 molecules^{-1} s^{-1}	R7	[40, 41]
N_2*	$N_2(A) + N_2$	→	$N_2 + N_2$	$k_8 = 3.000 \times 10^{-24}$ m^3 molecules^{-1} s^{-1}	R8	[37]
	$N_2(a) + N_2$	→	$N_2 + N_2$	$k_9 = 3.000 \times 10^{-24}$ m^3 molecules^{-1} s^{-1}	R9	[37]
	$N_2(a) + N_2$	→	$N_2(B) + N_2$	$k_{10} = 3.321 \times 10^{-46}$ m^3 molecules^{-1} s^{-1}	R10	[40, 41]
	$N_2(A) + N_2(A)$	→	$N_2 + N_2(B)$	$k_{11} = 3.321 \times 10^{-43}$ m^3 molecules^{-1} s^{-1}	R11	[40, 41]
	$N_2(A) + N_2(A)$	→	$N_2 + N_2(C)$	$k_{12} = 3.321 \times 10^{-43}$ m^3 molecules^{-1} s^{-1}	R12	[40, 41]
	$N_2(B) + N_2$	→	$N_2 + N_2$	$k_{13} = 1.661 \times 10^{-44}$ m^3 molecules^{-1} s^{-1}	R13	[40, 41]
	$N_2(B)$	→	N_2	$k_{14} = 1.661 \times 10^{-22}$ s^{-1}	R14	[40, 41]
	$N_2(C) + N_2$	→	$N_2 + N_2$	$k_{15} = 1.661 \times 10^{-44}$ s^{-1}	R15	[40, 41]
	$N_2(C) + N_2$	→	$N_2(B)$	$k_{16} = 4.151 \times 10^{-20}$ m^3 molecules^{-1} s^{-1}	R16	[40, 41]
	$N_2(A) + O_2$	→	$N_2 + O + O$	$k_{17} = 3.803 \times 10^{-39}$ m^3 molecules^{-1} s^{-1}	R17	[40, 41]
	$N_2(a) + O_2$	→	$N_2 + O + O$	$k_{18} = 3.803 \times 10^{-39}$ m^3 molecules^{-1} s^{-1}	R18	[40, 41]
	$N_2(C) + O_2$	→	$N_2 + O + O$	$k_{19} = 3.321 \times 10^{-39}$ m^3 molecules^{-1} s^{-1}	R19	[40, 41]
	$N_2(B) + O_2$	→	$N_2 + O + O$	$k_{20} = 3.321 \times 10^{-39}$ m^3 molecules^{-1} s^{-1}	R20	[40, 41]
H_2O	$e + H_2O$	→	$H + OH$	$k_{21} = 8.196 \times 10^{-15}$ m^3 molecules^{-1} s^{-1}	R21	[43]
	$H + OH + N_2$	→	$H_2O + N_2$	$k_{22} = 4.053 \times 10^{-43}$ m^6 molecules^{-2} s^{-1}	R22	[37]
	$H + OH + O_2$	→	$H_2O + O_2$	$k_{23} = 4.053 \times 10^{-43}$ m^6 molecules^{-2} s^{-1}	R23	[37]
	$O + H_2O$	→	$OH + OH$	$k_{24} = 4.250 \times 10^{-30}$ m^3 molecules^{-1} s^{-1}	R24	[37]
Zeldovich	$N_2 + O$	→	$NO + N$	$k_{25} = 1.051 \times 10^{-71}$ m^3 molecules^{-1} s^{-1}	R25	[47]
	$NO + N$	→	$N_2 + O$	$k_{26} = 3.331 \times 10^{-17}$ m^3 molecules^{-1} s^{-1}	R26	[47]
	$N + O_2$	→	$NO + O$	$k_{27} = 8.798 \times 10^{-23}$ m^3 molecules^{-1} s^{-1}	R27	[47]
	$NO + O$	→	$N + O_2$	$k_{28} = 6.772 \times 10^{-47}$ m^3 molecules^{-1} s^{-1}	R28	[47]
	$N + OH$	→	$NO + H$	$k_{29} = 1.836 \times 10^{-17}$ m^3 molecules^{-1} s^{-1}	R29	[47]
	$NO + H$	→	$N + OH$	$k_{30} = 3.239 \times 10^{-52}$ m^3 molecules^{-1} s^{-1}	R30	[47]
VOC	$C_7H_8 + O$	→	products	$k_{31} = 5.136 \times 10^{-20}$ m^3 molecules^{-1} s^{-1}	R31	[37]
	$C_7H_8 + OH$	→	products	$k_{32} = 2.231 \times 10^{-19}$ m^3 molecules^{-1} s^{-1}	R32	[37]
	$C_7H_8 + O_3$	→	products	$k_{33} = 6.119 \times 10^{-27}$ m^3 molecules^{-1} s^{-1}	R33	[37]

* The chemicals corresponding to $y_1, y_2, \ldots, y_{16}$ are as follows: O_2 (y_1), e (y_2), O (y_3), O_3 (y_4), N_2 (y_5), $N_2(A)$ (y_6), $N_2(a)$ (y_7), $N_2(B)$ (y_8), $N_2(C)$ (y_9), H_2O (y_{10}), H (y_{11}), OH (y_{12}), NO (y_{13}), N (y_{14}), C_7H_8 (y_{15}), products (y_{16}).

$$R_9: \quad \frac{dy_5}{dt} = k_9 y_7 y_5, \quad \frac{dy_7}{dt} = -k_9 y_7 y_5 \qquad (15), (16)$$

$$R_{10}: \quad \frac{dy_8}{dt} = k_{10} y_7 y_5, \quad \frac{dy_7}{dt} = -k_{10} y_7 y_5, \quad \frac{dy_5}{dt} = 0 \qquad (17), (18), (19)$$

$$R_{11}: \quad \frac{dy_8}{dt} = k_{11} y_6^{\,2}, \quad \frac{dy_6}{dt} = -2k_{11} y_6^{\,2}, \quad \frac{dy_5}{dt} = k_{11} y_6^{\,2} \qquad (20), (21), (22)$$

$$R_{12}: \quad \frac{dy_9}{dt} = k_{12} y_6^{\,2}, \quad \frac{dy_6}{dt} = -2k_{12} y_6^{\,2}, \quad \frac{dy_5}{dt} = k_{12} y_6^{\,2} \qquad (23), (24), (25)$$

$$R_{13}: \quad \frac{dy_8}{dt} = -k_{13} y_8 y_5, \quad \frac{dy_5}{dt} = k_{13} y_8 y_5 \qquad (26), (27)$$

$$R_{14}: \quad \frac{dy_8}{dt} = -k_{14} y_8, \quad \frac{dy_5}{dt} = k_{14} y_8 \qquad (28), (29)$$

$$R_{15}: \quad \frac{dy_9}{dt} = -k_{15} y_9 y_5, \quad \frac{dy_5}{dt} = k_{15} y_9 y_5 \qquad (30), (31)$$

$$R_{16}: \quad \frac{dy_9}{dt} = -k_{16} y_9, \quad \frac{dy_8}{dt} = k_{16} y_9 \qquad (32), (33)$$

$$R_{17}: \quad \frac{dy_6}{dt} = -k_{17} y_6 y_1, \quad \frac{dy_3}{dt} = 2k_{17} y_6 y_1, \quad \frac{dy_5}{dt} = k_{17} y_6 y_1 \qquad (34), (35), (36)$$

$$R_{18}: \quad \frac{dy_7}{dt} = -k_{18} y_7 y_1, \quad \frac{dy_3}{dt} = 2k_{18} y_7 y_1, \quad \frac{dy_5}{dt} = k_{18} y_7 y_1 \qquad (37), (38), (39)$$

$$R_{19}: \quad \frac{dy_9}{dt} = -k_{19} y_9 y_1, \quad \frac{dy_3}{dt} = 2k_{19} y_9 y_1, \quad \frac{dy_5}{dt} = k_{19} y_9 y_1 \qquad (40), (41), (42)$$

$$R_{20}: \quad \frac{dy_8}{dt} = -k_{20} y_8 y_1, \quad \frac{dy_3}{dt} = 2k_{20} y_8 y_1, \quad \frac{dy_5}{dt} = k_{20} y_8 y_1 \qquad (43), (44), (45)$$

H_2O:

$$R_{21}: \quad \frac{dy_{11}}{dt} = k_{21} y_2 y_{10} = \frac{dy_{12}}{dt}, \quad \frac{dy_{10}}{dt} = -k_{21} y_2 y_{10} \qquad (46), (47), (48)$$

$$R_{22}: \quad \frac{dy_{12}}{dt} = -k_{22} y_{11} y_{12} y_5 = \frac{dy_{11}}{dt}, \quad \frac{dy_{10}}{dt} = k_{22} y_{11} y_{12} y_5 = 0 \qquad (49), (50), (51)$$

$$R_{23}: \quad \frac{dy_{12}}{dt} = -k_{23} y_{11} y_{12} y_1 = \frac{dy_{11}}{dt}, \quad \frac{dy_{10}}{dt} = k_{23} y_{11} y_{12} y_1 = 0 \qquad (52), (53)$$

$$R_{24}: \quad \frac{dy_{12}}{dt} = 2k_{24} y_3 y_{10}, \quad \frac{dy_3}{dt} = -k_{24} y_3 y_{10}, \quad \frac{dy_{10}}{dt} = -k_{24} y_3 y_{10} \qquad (54), (55), (56)$$

Zeldovich reactions:

$$\mathrm{R}_{25}: \quad \frac{\mathrm{d}y_{13}}{\mathrm{d}t} = k_{25}y_5y_3 = \frac{\mathrm{d}y_{14}}{\mathrm{d}t}, \quad \frac{\mathrm{d}y_3}{\mathrm{d}t} = -k_{25}y_5y_3, \quad \frac{\mathrm{d}y_5}{\mathrm{d}t} = -k_{25}y_5y_3 \tag{57), (58), (59}$$

$$\mathrm{R}_{26}: \quad \frac{\mathrm{d}y_3}{\mathrm{d}t} = k_{26}y_{13}y_{14}, \quad \frac{\mathrm{d}y_{13}}{\mathrm{d}t} = -k_{26}y_{13}y_{14} = \frac{\mathrm{d}y_{14}}{\mathrm{d}t}, \quad \frac{\mathrm{d}y_5}{\mathrm{d}t} = k_{26}y_{13}y_{14} \tag{60), (61), (62}$$

$$\mathrm{R}_{27}: \quad \frac{\mathrm{d}y_{13}}{\mathrm{d}t} = k_{27}y_{14}y_1 = \frac{\mathrm{d}y_3}{\mathrm{d}t}, \quad \frac{\mathrm{d}y_{14}}{\mathrm{d}t} = -k_{27}y_{14}y_1 \tag{63), (64}$$

$$\mathrm{R}_{28}: \quad \frac{\mathrm{d}y_{14}}{\mathrm{d}t} = k_{28}y_{13}y_3, \quad \frac{\mathrm{d}y_{13}}{\mathrm{d}t} = \frac{\mathrm{d}y_3}{\mathrm{d}t} = -k_{28}y_{13}y_3 \tag{65), (66}$$

$$\mathrm{R}_{29}: \quad \frac{\mathrm{d}y_{13}}{\mathrm{d}t} = k_{29}y_{14}y_{12} = \frac{\mathrm{d}y_{11}}{\mathrm{d}t}, \quad \frac{\mathrm{d}y_{12}}{\mathrm{d}t} = -k_{29}y_{14}y_{12}, \quad \frac{\mathrm{d}y_{14}}{\mathrm{d}t} = -k_{29}y_{14}y_{12} \tag{67), (68), (69}$$

$$\mathrm{R}_{30}: \quad \frac{\mathrm{d}y_{14}}{\mathrm{d}t} = k_{30}y_{13}y_{11} = \frac{\mathrm{d}y_{12}}{\mathrm{d}t}, \quad \frac{\mathrm{d}y_{13}}{\mathrm{d}t} = \frac{\mathrm{d}y_{11}}{\mathrm{d}t} = -k_{30}y_{13}y_{11} \tag{70), (71}$$

VOC:

$$\mathrm{R}_{31}: \quad \frac{\mathrm{d}y_{16}}{\mathrm{d}t} = k_{31}y_{15}y_3, \quad \frac{\mathrm{d}y_{15}}{\mathrm{d}t} = \frac{\mathrm{d}y_3}{\mathrm{d}t} = -k_{31}y_{15}y_3 \tag{72), (73}$$

$$\mathrm{R}_{32}: \quad \frac{\mathrm{d}y_{16}}{\mathrm{d}t} = k_{32}y_{15}y_{12}, \quad \frac{\mathrm{d}y_{15}}{\mathrm{d}t} = \frac{\mathrm{d}y_{12}}{\mathrm{d}t} = -k_{32}y_{15}y_{12} \tag{74), (75}$$

$$\mathrm{R}_{33}: \quad \frac{\mathrm{d}y_{16}}{\mathrm{d}t} = k_{33}y_{15}y_4, \quad \frac{\mathrm{d}y_{15}}{\mathrm{d}t} = \frac{\mathrm{d}y_4}{\mathrm{d}t} = -k_{33}y_{15}y_4 \tag{76), (77}$$

2.3 Solving simultaneous ordinary differential equations (ODEs)

The fourth-order Runge–Kutta scheme described in Eqs. (78)–(85) is used for time integration of the ODEs (1)–(77).

$$\frac{\mathrm{d}y_\mathrm{i}}{\mathrm{d}t} = f\left(t, y_\mathrm{i}\right), \quad y_\mathrm{i}\left(t = t_0\right) = y_\mathrm{i}^0 \tag{78}$$

$$y_\mathrm{i}^{\mathrm{n+1}} = y_\mathrm{i}^{\mathrm{n}} + \frac{h}{6}\left(\Delta_{1\mathrm{i}} + 2\Delta_{2\mathrm{i}} + 2\Delta_{3\mathrm{i}} + \Delta_{4\mathrm{i}}\right), \quad \left(\mathrm{i} = 1,2,3,...,16\right) \tag{79}$$

$$y_\mathrm{i}^{\mathrm{n}} = y_\mathrm{i}\left(t_\mathrm{n}\right), \quad t_{\mathrm{n+1}} = t_\mathrm{n} + h \tag{80), (81}$$

$$\Delta_{1\mathrm{i}} = f\left(t_\mathrm{n}, y^\mathrm{n}\right) \tag{82}$$

$$\Delta_{2\mathrm{i}} = f\left(t^\mathrm{n} + \frac{h}{2}, y_\mathrm{i}^{\mathrm{n}} + \frac{h}{2}\Delta_{1\mathrm{i}}\right) \tag{83}$$

$$\Delta_{3i} = f\left(t^{n} + \frac{h}{2}, y_i^{n} + \frac{h}{2}\Delta_{2i} \right) \tag{84}$$

$$\Delta_{4i} = f\left(t^{n} + h, y_i^{n} + h\Delta_{3i} \right) \tag{85}$$

In this study, $f = f(y_i)$ (i = 1, 2,...), and f does not depend on t.

3. Calculation results and discussion

3.1 Direct plasma model and indirect plasma model (plasma injection model)

Two computational models are developed: a direct plasma model and an indirect plasma injection model. Both are implemented in Microsoft Excel Visual Basic for Application (Excel VBA) of Office 365. The parameters of the direct model are first calibrated against our reported experimental data, and the same parameters are then applied to the indirect model to predict the current experimental results. All simulation codes developed in this study are provided in the supplementary materials.

3.2 Results of the direct plasma model

Fig. 1 shows the dielectric barrier discharge (DBD) plasma reactor used in the Osaka Metropolitan University experiment [36]. The cylindrical barrier has an inner diameter of 0.02 m, a length of 0.265 m, a flow rate of 10 L min^{-1}, and a residence time of 0.5 s. A high voltage of 30 kV with a pulse frequency of f = 210 Hz is applied to generate plasma inside the cylinder. Toluene (C_7H_8) gas at a concentration of 60 ppm is introduced, and the resulting decomposition is measured.

The experimental results are presented in Fig. 2. The toluene concentration decreases from 60 to 4 ppm, while the ozone (O_3) concentration reaches 330 ppm at a specific energy (SE) of 2.667×10^{-2} kWh m^{-3} (red lines). These data are simulated using the direct plasma numerical model, with reaction rate coefficients listed in Table 1.

Calculations are performed using Excel VBA. The Excel VBA files with simulation procedure and parameter settings are provided in the supplementary materials. First, open the Excel file, display the "Developer" tab in Excel, and use the Excel VBA program displayed as a macro to enter the settings in red or blue character parts in the tab. Press the "Run" button to execute the macro, and the calculation results will be written into the table. If the Excel program remains in memory and cannot run, execute "tkill.bat" from the supplementary materials.

The features of the program and simulation are as follows. It is based on the calculation method described in previous chapters. The calculation uses a time step of 5×10^{-7} s (500 ns). Because a pulsed corona plasma is used, the pulse repetition frequency is set to 210 Hz, corresponding to $NTPON$ = 9,523, where T = 9,523 × 5×10^{-7} s. The electron density and the concentrations of N_2, O_2, and H_2O are held constant during the calculations.

The initial conditions are defined in the "init" tab of the Excel file named sim-inside-omu.xlsm" provided in the supplementary materials. The initial electron number density is set to $n_e = 9 \times 10^{15}$ m^{-3} based on previous calculations [40]. The simulated air flow is assumed to be at atmospheric pressure with 50% relative humidity (1.56% molar concentration), a gas temperature of 298 K, and an initial toluene concentration of 60 ppm. Reaction rate coefficients (k_1–k_{33}) are specified in the "conc" tab in the Excel file. Simulation parameters, including the time step (5×10^{-7} s), maximum number of time steps (1,000,000), maximum time (0.50 s), average flow rate (0.00016667 m^3 s^{-1}), and cross-sectional area (0.00031416 m^2), are also set in the same tab. The residence time of the gas inside the reactor is calculated as T_r = 0.500 s. The results are stored in the "conc" tab (in particles m^{-3}) and "ppm" tab (in ppm) as both tables and graphs, while the "g_rate" tab displays the generation rate (in particles m^{-3} s^{-1}). The results of the direct plasma calculations at the reactor outlet are as follows:

t = 0.5 s, O = 3.67 ppm, O_3 = 335 ppm, OH = 0.574 ppm, VOC (toluene, $C_6H_5CH_3$) = 4.05 ppm.

These values are in good agreement with the experimental results shown in Fig. 2. In this calculation, the reaction rate coefficient between toluene and O_3 is increased to 1.2×10^{-21} m^3 $molecule^{-1}$ s^{-1} to improve the agreement with experimental data. Toluene decomposition likely proceeds through reactions with O_3, O, and OH radicals, as well as through direct electron collisions. The relative contributions of these pathways are adjusted from an engineering design perspective. Fig. 2 depicts the transient behavior during the first 20 min after plasma application: the toluene concentration decreases, while ozone is generated and increases toward a quasi-steady level. Note that the kinetic model is a zero-dimensional well-mixed reactor model, and its main purpose is to predict the outlet concentrations; spatial concentration profiles along the reactor length are not considered. Using the results from "sim-inside-omu.xlsm", the calibrated parameters are applied to the indirect plasma model, which serves as the primary simulation target. Detailed results and graphical outputs are available in the "ppm" tab of the Excel file provided in the supplementary materials.

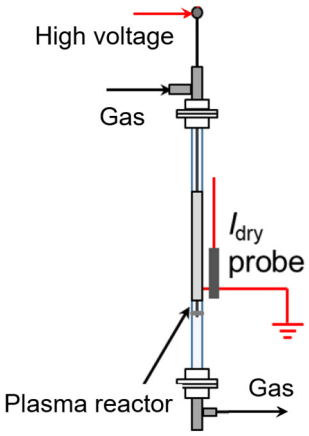

Fig. 1. Direct plasma reactor

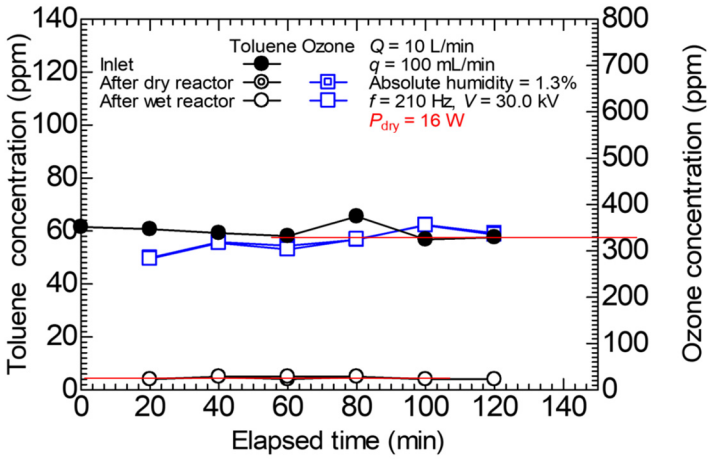

Fig. 2. Measurement result (SE = 2.667× 10^{-2} kWh/m^3, toluene concentration decreases from 60 to 4 ppm shown with the red lines, and O_3 = 330 ppm).

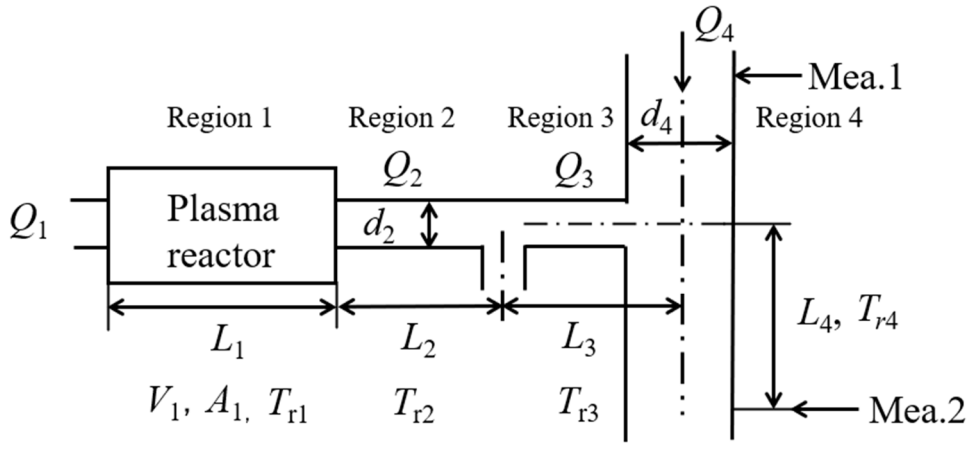

$$A_1,\ A_2 = A_3 = \pi d_2^2 / 4,\ A_4 = \pi d_4^2 / 4$$

$$V_1 = A_1 L_1,\ V_2 = A_2 L_2,\ V_3 = A_3 L_3,\ V_4 = A_4 L_4$$

$$T_{r1} = V_1 / Q_1,\ T_{r2} = V_2 / Q_2,\ T_{r3} = V_3 / Q_3,\ T_{r4} = V_4 / (Q_3 + Q_4)$$

Fig. 3. Four regions with lengths L_1, L_2, L_3, and L_4 in the calculation of the indirect plasma model.

3.3 Results of the indirect plasma model (calculation target) and discussion

In the current calculation for the indirect plasma (plasma injection) model, the flow domain is divided into four regions of lengths L_1, L_2, L_3, and L_4, as illustrated in Fig. 3. The system configuration is as follows:

Region 1: DBD plasma reactor through which air flows at a flow rate, Q_1; reactor length, cross-sectional area, and residence time are L_1, A_1, and T_{r1}, respectively.

Region 2: Tubular channel with diameter d_2 carrying gas at a flow rate, Q_2; pipe length, cross-sectional area, and residence time are L_2, A_2, and T_{r2}, respectively.

Region 3: Tubular channel with diameter d_2 conveying gas at a flow rate, Q_3. A branch pipe between Q_2 and Q_3 is installed to investigate how the injection flow rate Q_3 affects the VOC decomposition efficiency in the experiments. Q_3 becomes equal to Q_2, or smaller than Q_2 by the branch pipe flow; pipe length, cross-sectional area, and residence time are L_3, $A_3 = A_2$, and T_{r3}, respectively. Plasma-treated gas of the flow rate Q_3 is injected into Region 4 to treat the VOC.

Region 4: Tubular channel with inner diameter d_4 conveying gas at a flow rate, Q_4; pipe length, cross-sectional area, and residence time are L_4, A_4, and T_{r4}, respectively. The VOC (allyl disulfide) - containing air flows at a rate of Q_4 and passes through the pipe of the region, where VOC is treated by the plasma-treated gas injection. VOC concentrations are measured at two points (Mea. 1 and Mea. 2).

Note that regarding the plasma decomposition of toluene, the byproducts after the reaction can be identified and quantified using FTIR [36]. However, because there is no information available on allyl disulfide, byproducts are listed collectively as products.

Fig. 4 shows a schematic of the concentration changes of the VOC and radicals in the four regions used in the calculation of the indirect plasma model. The horizontal axis represents time, and the vertical axis represents the concentration of species. Simulations are performed corresponding to experimental cases Nos. 1, 2, and 4, explained below.

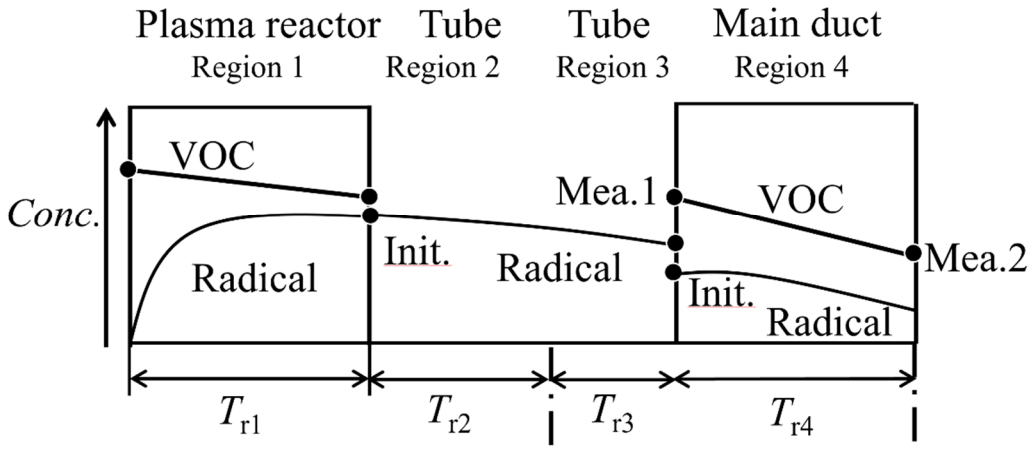

Fig. 4. Schematic of VOC concentration changes and radicals in the four calculation regions of the indirect plasma model.

Region 1 (residence time = T_{r1}) is located inside the DBD plasma reactor. Calculations are performed with the Excel file named "sim-inside-Tr1.xlsm" provided in the supplementary materials. Air flows in at a rate, Q_1 (= 4.9 m³ min^{-1}) at 8.2 kV with a frequency f = 10 kHz. The voltage is a sinusoidal wave with a power density (SE) of 1.36 × 10^{-3} kWh m^{-3}, 400 W power, a rectangular cross-sectional area, A_1 = 6.88 × 10^{-3} m^2, and a reactor length L_1 = 0.04 m. The average electron temperature ratio, calculated using the empirical relation, $n_e \sim SE / T_e$, is assumed to be 1.274. As such, n_e = 1.36 ×10^{-3}/2.667×10^{-2} × 1.274 × 9 ×10^{15} = 5.85 ×10^{14} m^{-3}. We also assume a pulse number N_NTPON = 50, T = 50 × 5 × 10^{-7} s = 2.5× 10^{-5} s, and that four pulses occur in one period, f = 1 / T / 4 = 10 kHz. The calculations are performed at a residence time T_{r1} = 0.00335 s. Because a zero concentration cannot be accommodated in the calculation, 1,000 m^{-3} = 4.06 × 10^{-17} ppm is regarded as the minimum or zero concentration. Detailed calculation results are presented as graphs in the "ppm" tab of the Excel file. The concentrations of the main components at the outlet are as follows:

t = 0.0035 s, O = 0.277 ppm, O_3 = 31.8 ppm, OH = 2.41 ppm, and N = 0 ppm.

Region 2 (residence time = T_{r2}) is a tubular channel with a circular cross-section and diameter d_2 = 0.1 m. Calculation is performed with the Excel file named "sim-outside-Tr2.xlsm" provided in the supplementary materials. The gas flows into the channel at a rate of $Q_2 = Q_1$ = 4.9 m³ min^{-1}. The cross-sectional area A_2 = 7.85 × 10^{-3} m^2, and the length L_2 = 0.8 m. The initial concentrations of the components are set as the final concentrations at the exit of Region 1 in the "init" tab of the Excel file. Calculations are performed for a residence time of T_{r2} = 0.07692 s in the channel. At the outlet, the concentrations of active species such as O, OH, and N nearly completely decay, and the concentration of O_3 slightly increases to O_3 = 32.1 ppm. It is considered that O formed by excited N_2 species recombines after the outflow, and the concentration of O_3 increases. For detailed results, refer to the calculation results and graphs in the "ppm" tab of the Excel file. The concentrations of the main components at the outlet are as follows:

t = 0.07692 s, O = 0 ppm, O_3 = 32.1 ppm, OH = 0.052 ppm, and N = 0 ppm.

Region 3 (residence time T_{r3}) is a tubular channel with a circular cross-section and diameter d_3 = 0.1 m. Calculations are performed using the Excel files named "sim-outside-Tr3-No1.xlsm" and "sim-outside-Tr3-Nos3-4.xlsm" provided in supplementary materials. Three cases are analyzed: Cases Nos. 1, 3, and 4. Case No. 2 is excluded because no plasma treatment was applied. In Case No. 1, the gas flows through the channel at $Q_3 = Q_2$ = 4.9 m³ min^{-1} with the branch-pipe exit closed. For Cases Nos. 3 and 4, the flow rate decreased to Q_3 = 1.2 m³ min^{-1} due to outflow from the branch-pipe exit. The cross-sectional area and reactor length are A_3 = 7.85 × 10^{-3} m² and L_3 = 0.6 m, respectively. The initial concentrations of the components are set as the final concentrations at the exit of Region 2 in the "init" tab of the Excel files. Calculations were performed up to residence times of T_{r3} = 0.05770 s (Case No. 1) and T_{r3} = 0.23562 s (Cases Nos. 3 and 4). At the outlet, all active species except O_3 have nearly decayed to zero, while the O_3 concentration remains nearly constant. Detailed results and graphs are provided in the "ppm" tab of the Excel files. The concentrations of the main components at the outlet are as follows:

No. 1: t = 0.0577 s, O = 0 ppm, O_3 = 32.1 ppm, OH = 0.030 ppm, and N = 0 ppm.

No. 3 and No. 4: t = 0.0577 s, O = 0 ppm, O_3 = 32.1 ppm, OH = 0.013 ppm, and N = 0 ppm.

Region 4 (residence time = T_{r4}) is a channel with a larger circular cross-section (d_4 = 0.2 m) where the flow from the plasma reactor merges with the mainstream. Calculations are performed using the Excel files named "sim-outside-Tr4-No1.xlsm", "sim-outside-Tr4-No3.xlsm", and "sim-outside-Tr4-No4.xlsm" provided in the supplementary materials. The combined flow rates are $Q_3 + Q_4$ = 11.6 m^3 min^{-1} (Case No. 1) and 12.8 m³ min^{-1} (Cases Nos. 3 and 4), corresponding to dilution ratios Q_3/Q_4 of 0.422 and 0.0938, respectively. Experiments were conducted to investigate how the dilution ratio affects the VOC removal efficiency. The channel dimensions are A_4 = 3.14 × 10^{-3} m² and L_4 = 2.0 m. Allyl disulfide ($C_6H_{10}S_2$) vapor, representing the target VOC, is introduced at the inlet with concentrations of 0.435 and 0.595 ppm at measurement point Mea. 1, while downstream (Mea. 2) concentrations were 0.097–0.099 ppm. Because the reaction rate coefficient for allyl disulfide is not reported by NIST, the coefficient for toluene (k = 9.3 × 10^{-20} m³ molecule^{-1} s^{-1}) was used initially. The reaction rate constant for allyl disulfide with ozone is assumed to be higher (k_{33} = 6.119 × 10^{-27} m³ molecule^{-1} s^{-1}). The initial concentrations of the components are set as the final concentrations at the exit of Region 3 in the "init" tab of the Excel files. Calculations are performed up to a residence time of T_{r4} = 0.29453 s. Detailed results and graphs are provided in the "ppm" tab of the Excel files. The concentrations of the main components at Mea. 2 are as follows:

No. 1: t = 0.29453 s, O = 0 ppm, O_3 = 13.0 ppm, OH = 0.0566 ppm, N = 0 ppm, and VOC = 3.1 × 10^{-5} ppm.

No. 3: t = 0.29453 s, O = 0 ppm, O_3 = 2.5 ppm, OH = 0.000730 ppm, N = 0 ppm, and VOC = 0.0973 ppm.

No. 4: t = 0.29453 s, O = 0 ppm, O_3 = 2.6 ppm, OH = 0.000824 ppm, N = 0 ppm, and VOC = 0.0671 ppm.

Table 2 presents the results of the comparison between the experimental (Exp.) and calculated (Cal.) trials for O_3 outlet concentration, VOC inlet/outlet concentrations, and VOC removal efficiency. A good agreement is observed between the calculated and experimental results.

Table 2. Comparison of experimental and calculated results of cases, O_3 outlet concentrations, VOC inlet/outlet concentrations of allyl disulfide, and removal efficiencies.

Case No.	O_3 outlet Exp. ppm	O_3 outlet Cal. ppm	VOC inlet Exp. ppm	VOC outlet Exp. ppm	VOC outlet Cal. ppm	VOC removal efficiency Exp. %	VOC removal efficiency Cal. %
1	−	13.0	0.533	0.099	0.000304	81.4	99.9
3	2.4	2.5	0.595	0.097	0.0973	83.6	83.6
4	2.4	2.6	0.435	0.098	0.0671	77.5	84.6

Note that we are confident that for the present scope—an ODE system comprising 33 reactions under the investigated operating conditions—Excel/VBA can be used effectively and offers a practical, accessible implementation for engineering analysis. To improve numerical accuracy and stability, we used a sufficiently small-time step and confirmed convergence. In addition, as a further verification step, we plan to cross-check the results in future work using a standard stiff ODE solver such as the C-based Variable-coefficient Ordinary Differential Equation solver (CVODE) and/or Scientific Python (SciPy). Furthermore, it has been pointed out that OH in humid-air DBDs typically decays on sub-millisecond timescales, whereas our model predicts an OH tail persisting through regions with residence times of 0.05–0.29 s (e.g., OH = 0.0566 ppm at the Region 4 outlet for Case No. 1). It has also been noted that the complete decay of O atoms by Region 2 may appear inconsistent with literature reports in which DBD-generated O can persist for ~1–10 ms, depending on humidity and wall conditions. These differences may stem from simplifications in the present model, such as assuming constant e^-, O_2, N_2, and H_2O, omitting wall reactions and diffusion losses, and/or uncertainties in selected rate constants (e.g., for R5, R23, R24, and R25). More detailed simulation should be future work.

4. Conclusions

To build foundational knowledge for designing and optimizing volatile organic compound (VOC) abatement devices, we conducted integrated numerical simulations and laboratory experiments on VOC removal using both direct and indirect nonthermal plasma injection methods. The main findings, consistent across both approaches, are summarized below.

(1) The plasma injection method is successfully simulated, and the predicted behaviors closely reproduced experimental trends. The responses of the model are sufficiently accurate to be considered predictive under the present conditions, demonstrating strong agreement between simulation and experiment.
(2) Under the adopted conditions, the ozone (O_3) concentration at the plasma-device outlet increased by approximately 0.3 ppm. This increase results from the recombination of oxygen radicals (O) formed through N_2 excitation, consistent with the modeled species balances.
(3) After injection, the O_3 concentration remains nearly constant along the flow path to the outlet but decreased with higher dilution rates and VOC reactivity. Thus, mixing intensity and subsequent VOC chemistry control the downstream evolution of O_3.
(4) Atomic oxygen (O) and nitrogen (N) concentrations decline rapidly after injection, indicating short lifetimes for these reactive species. In contrast, hydroxyl radicals (OH) decay more slowly, reflecting distinct kinetic pathways and radical stability.
(5) The decomposition efficiency of allyl disulfide ($C_6H_{10}S_2$) is accurately reproduced by adjusting the relevant reaction rate constant within reasonable limits. This calibration yields degradation trends consistent with the experiment, supporting the reliability of the reaction mechanism.
(6) Future work will examine conditions that enhance N_2 excitation, focusing on the role of moisture. By varying humidity from the current 50% relative level and refining additional model parameters, we aim to quantify humidity sensitivity and strengthen the model's predictive robustness of the model.

References

[1] Shimada T., Yamasaki H., Kuroki T., Kang J., Kim D.W., Yagi T., and Okubo M., Wet-type packed-bed nonthermal plasma for simultaneous removal of PM and VOCs, *Plasma Chem. Plasma Process*., Vol. 44, pp. 239–255, 2024.

[2] Shayegan Z., Haghighat F., and Lee C.S., Photocatalytic oxidation of volatile organic compounds for indoor environment applications: Three different scaled setups, *Chem. Eng. J*., Vol. 357, pp. 533–546, 2019.

[3] Liotta L. F., Catalytic oxidation of volatile organic compounds on supported noble metals, *Appl. Catal. B*, Vol. 100, pp. 403–412, 2010.

[4] Xin Y. Ando Y., Nakagawa S., Nishikawa H., and Shirai T., New possibility of hydroxyapatites as noble-metal-free catalysts towards complete decomposition of volatile organic compounds, *Catal. Sci. Technol*., Vol. 10, pp. 5453–5459, 2020.

[5] Zhang X., Gao B., Creamer A.E., Cao C., and Li Y., Adsorption of VOCs onto engineered carbon materials: A review. *J. Hazard. Mater*., Vol. 338, pp. 102–123, 2017.

[6] Cheng Y., He H., Yang C., Zeng G., Li X., Chen H., and Yu G.L., Challenges and solutions for biofiltration of hydrophobic volatile organic compounds, *Biotechnol. Adv.*, Vol. 34, pp. 1091–1102, 2016.

[7] Urashima K., and Chang J. S., Removal of volatile organic compounds from air streams and industrial flue gases by non-thermal plasma technology, *IEEE Trans. Dielectr. Elect. Insul.*, Vol. 7, pp. 602–610, 2000.

[8] Kohno H., Berezin A. A., Chang J. S., Tamura M., Yamamoto T., Shibuya A., and Hondo S., Destruction of volatile organic compounds used in a semiconductor industry by a capillary tube discharge reactor, *IEEE Trans., Ind. Appl*., Vol. 34, pp. 953–966, 1998.

[9] Oda T., Takahashi T., and Yamaji K., Nonthermal plasma processing for dilute VOCs decomposition, *IEEE Trans. Ind. Applicat*., Vol. 38, pp. 873–878, 2002.

[10] Shibata T. and Nishiyama H., Acetic acid decomposition in a coaxial dielectric barrier discharge tube with mist flow, *Plasma Chem. Plasma Process*., Vol. 34, pp. 1331–1343, 2014.

[11] Kuroki T., Nishii S., Kuwahara T., and Okubo M., Nanoparticle removal and exhaust gas cleaning using gas-liquid interfacial nonthermal plasma, *J. Electrostat*., Vol. 87, pp. 86–92, 2017.

[12] Takehana K., Kuroki T., and Okubo M., Evaluation on nitrogen oxides and nanoparticle removal and nitrogen monoxide generation using a wet-type nonthermal plasma reactor, *J. Phys. D: Appl. Phys*., Vol. 51, 204002, 2018.

[13] Yamasaki H., Nomura S. Xun X., Kuroki T., Kang J., Yagi T., and Okubo M., Toward NO_x/SO_x and nanoparticle control technology using a single-stage wet-type nonthermal plasma reactor, *IEEE Trans. Plasma Sci*., Vol. 49, pp. 1860–1870, 2021.

[14] Kim S.H., Lee G., Park J.H. Choi Y., Kang K., Kwak S., and Kim H.J., Optimizing air purification systems in subway stations: Case study of fine particulate matter reduction at Yeongtong station, *Int. J. Plasma Environ. Sci. Technol*., Vol. 19 (2), e02020 (8pp), 2025.

[15] Mochinaga K., Furuki, T., Tachibana K., Ichiki R., Kanazawa S., Tański M., Kocik M., and Mizeraczyk J., Development of compact electrostatic precipitator using EHD gas pump mechanism, *Int. J. Plasma Environ. Sci. Technol*., Vol. 19 (1), e01002 (7pp), 2025.

[16] Zukeran A., Mashimo F., Kihara S., Yasumoto K., Wada R., Takamura T., Sawai J., and Ehara, Y., Collection of nano size particle and airborne virus in an electrostatic precipitator with carbon brush disk electrode, *Int. J. Plasma Environ. Sci. Technol*., Vol. 19 (2), e02002 (9pp), 2025.

[17] Tanino T., Matsui M., Kogure K., and Ohshima T., Collection and inactivation of airborne microorganisms using combination of water trap and electrical technologies, *Int. J. Plasma Environ. Sci. Technol*., Vol. 16 (1), e01002 (8pp), 2022.

[18] Moreau E., Souakri S., Bellanger R., and Benard N., Ionic wind produced by a millimeter-gap DC corona discharge ignited between a plate and an inclined needle, *Int. J. Plasma Environ. Sci. Technol.*, Vol. 15 (1), e01001 (15pp), 2021.

[19] Terasawa K., Sugiyama H., Ikeda Y., Wada R., Sawai J., Ohguri N., Asada T., Matsumoto N., Yamashiro K., and Zukeran A., Collection efficiency of ultrafine particles and inactivation of microorganisms under low ozone concentration in an electrostatic precipitator, *Int. J. Plasma Environ. Sci. Technol.*, Vol. 15 (3), e03005 (12pp), 2021.

[20] Podliński J., Berendt A., and Mizeraczyk J., Particle image velocimetry measurements of airflow in an electrohydrodynamic device for air cleaning, *Int. J. Plasma Environ. Sci. Technol*., Vol. 7 (1), pp. 82–88, 2013.

[21] Ehara Y., Nakano R., Yamamoto T., Zukeran A., Inui T., and Kawakami H., Performance of high-velocity electrostatic precipitator for road tunnels, *Int. J. Plasma Environ. Sci. Technol.*, Vol. 5 (2), pp. 157–160, 2011.

[22] Gouri R., Zouzou N., Tilmatine A., Moreau E., and Dascalescu L., Collection Efficiency of a DBD Electrostatic Precipitator under Different High Voltage Waveforms, *Int. J. Plasma Environ. Sci. Technol*., Vol. 5 (2), pp. 191–195, 2011.

[23] Jiang N., Li J., Hu L., Zhai W., Shang K., Lu N., and Wu Y., Optimization investigation on geometrical parameters of a multistage asymmetric fin-type DBD reactor for improved degradation of toluene, *Int. J. Plasma Environ. Sci. Technol*., Vol. 14 (3), e03002 (9pp), 2020.

[24] Torigoe Y., Iwasaki A., Namihira T., and Wang D., Ethylene decomposition by nanosecond pulsed discharge and evaluation of by-products, *Int. J. Plasma Environ. Sci. Technol*., Vol. 12 (2), pp. 114–119, 2019.
[25] Zhang X., Chen W., Zhu J., Feng W., and Yan K., Aerosol formation and decomposition of benzene derivatives by AC/DC streamer corona discharge, *Int. J. Plasma Environ. Sci. Technol*., Vol. 4 (2), pp. 130–134, 2010.
[26] Kacprzyk R., Mista W., and Czapka T., Atmospheric pressure cold plasma reactor with back discharges and parallel gas flow," *Int. J. Plasma Environ. Sci. Technol*., Vol. 5 (1), pp. 58–61, 2011.
[27] Kuroki T., Tanaka T., and Okubo M., Decomposition of toluene adsorbed on hydrophobic media by nonthermal plasma flow with water spray, *Int. J. Plasma Environ. Sci. Technol*., Vol. 11 (1), pp. 92–97, 2017.
[28] Kim H. -H. and Ogata A., Interaction of nonthermal plasma with catalyst for the air pollution control, *Int. J. Plasma Environ. Sci. Technol*., Vol. 6 (1), pp. 43–48, 2012.
[29] Maciuca A., Batiot-Dupeyrat C., and Tatibouët J.M., Coupling non-thermal plasma with photocatalysis for VOC abatement: A review, *Int. J. Plasma Environ. Sci. Technol*., Vol. 6 (2), pp. 135–139, 2012.
[30] van Heesch E. J. M., Yan K., Pemen A. J. M., Winands G. J. J., Beckers F. J. C. M., and Hoeben W. F. L. M., From pulsed power to processing: plasma initiated chemical process intensification, *Int. J. Plasma Environ. Sci. Technol*., Vol. 6 (2), pp. 87–92, 2012.
[31] Watanabe S., Ida J., Matsuyama T., and Yamamoto H., Application of SPCP (Surface corona discharge induced plasma chemical process) reactor system to water treatment, *Int. J. Plasma Environ. Sci. Technol*., Vol. 4 (1), pp. 31–35, 2010.
[32] Shimizu K., Kanamori M., and Blajan M., Application of atmospheric microplasma for indoor air treatment, *Int. J. Plasma Environ. Sci. Technol*., Vol. 4 (1), pp. 45–51, 2010.
[33] Vandenbroucke A., Morent R., De Geyter N., Nguyen Dinh M.T., Giraudon J.-M., Lamonier J.-F., and Leys C., Plasma-catalytic decomposition of TCE, *Int. J. Plasma Environ. Sci. Technol*., Vol. 4 (2), pp. 135–138, 2010.
[34] Oda T., Kuramochi H. and Ono R. Trichloroethylene decomposition by the nonthermal plasma combined with manganese-dioxide supported alumina, *Int. J. Plasma Environ. Sci. Technol*., Vol. 2 (1), pp. 50–55, 2008.
[35] Kim H.H., Kim J.H., and Ogata A., Adsorption and oxygen plasma-driven catalysis for total oxidation of VOCs, *Int. J. Plasma Environ. Sci. Technol*., Vol. 2 (2), pp. 106–112, 2008.
[36] Shibata R., Ushida R., Okabe K., Yamasaki H., Kuroki T., and Okubo M., Dry and wet hybrid plasma treatment for volatile organic compound removal, *J. Hazard. Mater*., 2025, submitted.
[37] NIST Chemical Kinetics Database, National Institute of Standards and Technology, https://kinetics.nist.gov/ (accessed April 11, 2025).
[38] Ikebe K., Nakanishi K., Arai S., Evolution process of microdischarge products in ozonizer, *Trans. IEE Japan*, Vol. 109-A (11), pp. 474–480, 1989. (in Japanese)
[39] Okubo M., Yoshida K., and Yamamoto T., Numerical and experimental analysis of nanosecond pulse dielectric barrier discharge-induced nonthermal plasma for pollution control, *IEEE Trans. Ind. Applicat*., Vol. 44 (5), pp. 1410–1416, 2008.
[40] Shimada T., Yamasaki H., and Okubo M., Evolution of streamer groups and radical generation in high-voltage multiple-pulse-induced nonthermal plasma, *Phys. Plasmas*, Vol. 30 (10), 103508, 2023.
[41] Okubo M., Fundamentals and applications of nonthermal plasma fluid flows: A review, *Plasma*, Vol.6 (2), pp. 277–307, 2023.
[42] Song M.Y., Cho H., Karwasz G.P., Kokoouline V., Nakamura Y., Tennyson J., Faure A., Mason N.J., and Itikawa Y., Cross sections for electron collisions with H_2O, *J. Phys. Chem. Ref. Data*, Vol. 50, 023103, 2021.
[43] Itikawa Y., and Mason N., Cross sections for electron collisions with water molecules, *J. Phys. Chem. Ref. Data*, Vol. 34 (1), pp. 1–22, 2005.
[44] Itikawa Y., Cross sections for electron collisions with nitrogen molecules, *J. Phys. Chem. Ref. Data*, Vol. 35 (1), pp. 31–53, 2006.
[45] Kogelschatz U., Dielectric-barrier discharges: Their history, discharge physics, and industrial applications, *Plasma Chem. Plasma Process*., Vol. 23 (1), pp. 1–46, 2003.
[46] Taguchi M., Ozone zero phenomenon in ozone generator equipped with coaxial cylinder electrodes covered by dielectrics, *IEEJ Trans. Fundamentals and Materials A*, Vol. 134 (4), pp. 279–284, 2014. (in Japanese)
[47] Aithal S. M., A comparative study of NO_x computation methods coupled to quasi-dimensional models in SI engines, *Proc. ASME 2012 ICE Division Fall Technical Conference*, Vancouver, Canada, Sept. 23–26, 2012. https://doi.org/10.1115/ICEF2012-92012
[48] Kansai Ozone Technology Study Group, Reaction of ozone (4): reaction rate constants, *Technical Note*, No. 43, 2015 (in Japanese); https://www.k-ozone.org/
[49] Roh S.A., Han S.Y., Lee D.H., Kim K.-T., and Song H., Ozonation of styrene in the flue gas from fiberglass reinforced plastics manufacturing facility: Laboratory and on-site studies, *Korean J. Chem. Eng*., Vol. 40 (5), pp. 1116–1121, 2023.
[50] Arai N., Higashi T., Hasatani M., and Sugiyama S., Formation of thermal NO_x in binary system of nitrogen-oxygen, *Kagaku Kogaku Ronbunsyu*, Vol. 3 (3), pp. 243–247, 1977. (in Japanese)

[51] Takeuchi N., Comparison of one- and zero-dimensional reaction models of liquid-phase radicals for plasma generated on gas-liquid interface, *IEEJ Trans. Fund. Mat., Part A*, Vol. 134 (5), pp. 315–320, 2014.
[52] Tabata N., Tanaka M., and Yagi S., The characteristics of ozone generation from air as compared with from oxygen by silent discharge ozonizer, *Trans. Inst. Electr. Eng. Jpn.*, *Part B*, Vol. 97 (11), pp. 665–672, 1977. (in Japanese).
[53] Iijima T., Makise R., and Murata T., OH radical generator for waste water treatment containing recalcitrant organic matter, *Toshiba Review*, Vol. 61 (8), pp. 40–42, 2006. (in Japanese)
[54] Yang X., Shen X., Zhao P., and Law C.K., Statistical analysis on rate parameters of the H_2–O_2 reaction system, *J. Phys. Chem. A*, Vol. 125 (47), pp. 10223–10234, 2021.
[55] The Engineering Toolbox, Moist Air – Water Vapor and Saturation Pressure, (Online). Available: https://www.engineeringtoolbox.com/water-vapor-saturation-pressure-air-d_689.html (Accessed: Apr. 11, 2025).
[56] Ishii S., Gas discharges at atmospheric pressure region, Journal of Plasma and Fusion Research, Vol. 70 (1), pp. 61–66, 1994. (in Japanese)

International Journal of
Plasma Environmental Science and Technology

Supporting Information

Supplementary materials

The following supplementary materials can be downloaded at: https://www.osakam-u.com/plasma/ijpest/supplementary/25-10/all.zip.

Region inside the Osaka Metropolitan University reactor: sim-inside-omu.xlsm; Region 1 inside the plasma reactor: sim-inside-Tr1.xlsm; Region 2 outside the plasma reactor: sim-outside-Tr2.xlsm; Region 3 outside the plasma reactor, No.1 condition: sim-outside-Tr3-No1.xlsm; Region 3 outside the plasma reactor, Nos.3-4 conditions: sim-outside-Tr3-Nos3-4. xlsm; Region 4 outside the plasma reactor, No.1 condition: sim-outside-Tr4-No1.xlsm; Region 4 outside the plasma reactor, No.3 condition: sim-outside-Tr4-No3.xlsm; Region 4 outside the plasma reactor, No.4 condition: sim-outside-Tr4-No4.xlsm; Batch file for stopping unterminated VBA program: taskkill.bat